GSA DATA REPOSITORY 2014243 Arnulf et al.

SUPPLEMENTARY MATERIAL

Data Analysis

Downward continuation (Berryhill, 1984; Arnulf et al., 2014) can be used to transform the MCS data to simulate a different acquisition geometry, for example, to move seismic source and receiver positions from the sea surface to a new datum at or near the seafloor, simulating an on-bottom refraction experiment. This process essentially unwraps the layer 2A/2B triplication, moving the refracted energy in front of the seafloor reflection. In this study, the downward continuation of both shots and receivers using the Kirchhoff integral formulation (Berryhill, 1984) created a simulated experiment 75 m above the seafloor.

Full Waveform Inversion (FWI) is used in iterative attempts to match synthetically calculated seismograms with observed waveforms. It is a data-driven form of analysis that leads to high-resolution imaging by extracting quantitative information from the seismograms. The inversion algorithm used in this study was originally developed by Tarantola (1986) and implements the 2D elastic wave equation using a staggered-grid finite difference scheme with second-order accuracy in time and fourth-order accuracy in space (Levander, 1988). Waveform inversion in this study was designed to principally targeted the energy related to P-wave refraction events and some wide-angle reflections present in the downward continued MCS data. We followed a multi-stage FWI strategy alternating between model updates, where we inverted simultaneously for Vp and Vs, and source updates. No attenuation was included in the modeling. Preprocessing of the field data was accomplished during the downward continuation stage. A seventh-order Butterworth band-pass filter with corner frequencies of 3 and 15 Hz was first applied to constrain the frequencies of the downward continued data to ones that satisfy the stability criterion of a 12.5 m finite-difference grid. Second, the observed signal was convolved by $H(t)/\sqrt{t}$ (H being the Heaviside step function and t being the time) to better simulate a 2-D experiment and boost low frequencies with respect to high frequencies. Finally a predictive deconvolution filter was also designed to minimize the bubble pulse effect.

Reverse-Time Migration (RTM, Baysal et al, 1983) is a prestack two-way wave-equation migration technique for accurate imaging in and below areas with great structural and velocity complexities. RTM computes full two-way numerical solutions to the wave equation. As such, it has no dip limitation and it handles extreme lateral velocity variations using all possible arrivals. The modeling scheme implemented within our RTM algorithm is the same as the one used for the FWI. The RTM P-wave velocity gradient images presented in this paper are evaluated in terms of the normal stresses of the forward source wavefield ($\overrightarrow{\tau_{xx}}, \overrightarrow{\tau_{zz}}$) and normal stresses of the reverse time data wavefield ($\overleftarrow{\tau_{xx}}, \overleftarrow{\tau_{zz}}$) according to:

$\delta\hat{\alpha}_{RTM} = -\frac{\rho\alpha}{2(\lambda+\mu)^2}\sum_{shots}\int_0^T dt(\overleftarrow{\tau_{xx}} + \overleftarrow{\tau_{zz}})(\overrightarrow{\tau_{xx}} + \overrightarrow{\tau_{zz}})$, (see: Shipp and Singh, 2002),

where ρ is the density, α is the P-wave velocity, λ and μ are the Lamé parameters and the equation is integrated over time. Preprocessing of the sea surface field data included a seventh-order Butterworth band-pass filter with corner frequencies of 3 and 30 Hz to constrain the frequencies of the sea surface data to ones that satisfy the stability criterion of a 6.25 m finite-difference grid. Convolution using the $H(t)/\sqrt{t}$ function as well as a predictive deconvolution filter were also applied.

References Cited

Arnulf, A.F., Harding, A.J., Kent, G.M., Singh, S.C., and Crawford, W., 2014, Constraints on the shallow velocity structure of the Lucky Strike Volcano, Mid-Atlantic Ridge, from downward continued multichannel streamer data: J. Geophys. Res., in press.

Baysal, E., Kosloff, D.D., 1983, and Sherwood, J.W.C. Reverse time migration: Geophysics, v. 48, p. 1514-1524.

Berryhill, J.R., 1984, Wave□equation datuming before stack: Geophysics, v. 49, p. 2064–2066, doi:10.1190/1.1441620.

Levander, A.R., 1988, Fourth-order finite-difference P-SV seismograms: Geophysics, v. 53, p. 1425–1436.

Shipp, R.M., and Singh, S.C., 2002, Two-dimensional full wavefield inversion of wide-aperture marine seismic streamer data, v. 151, p. 325-344.

Tarantola, A., 1986, A strategy for nonlinear elastic inversion of seismic reflection data: Geophysics, v. 51, p. 1893-1903.

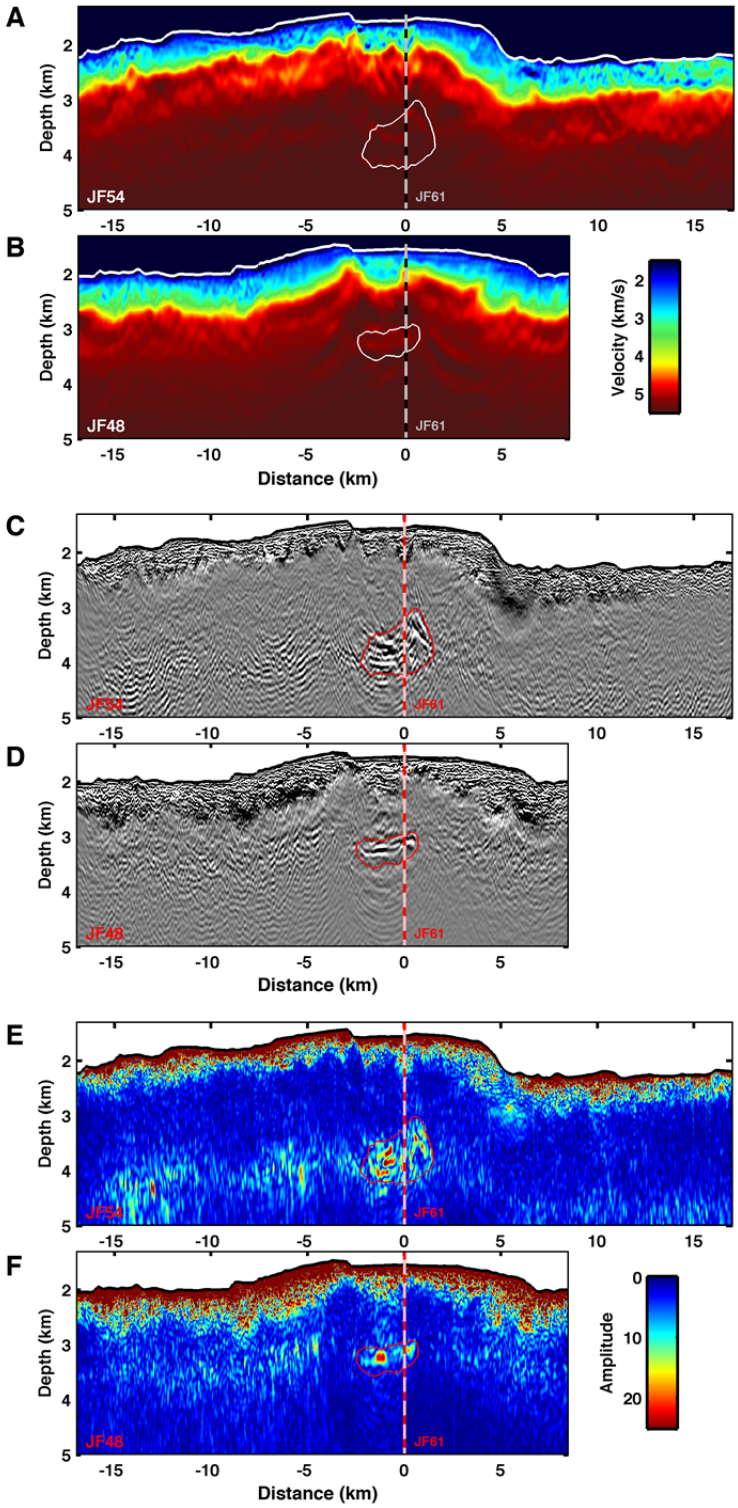

Figure DR1. Upper crustal velocity, reflectivity and amplitude structure of Axial volcano along seismic lines 54 (top panel) and 48 (bottom panel). A, B: P-wave velocity sections. C, D: Reverse time migrated images. E, F: Amplitude envelope of the reverse time migrated images. White lines (A, B) and red lines (C, D, E and F) outline the main crustal magma reservoir and were identified from the RTM images.

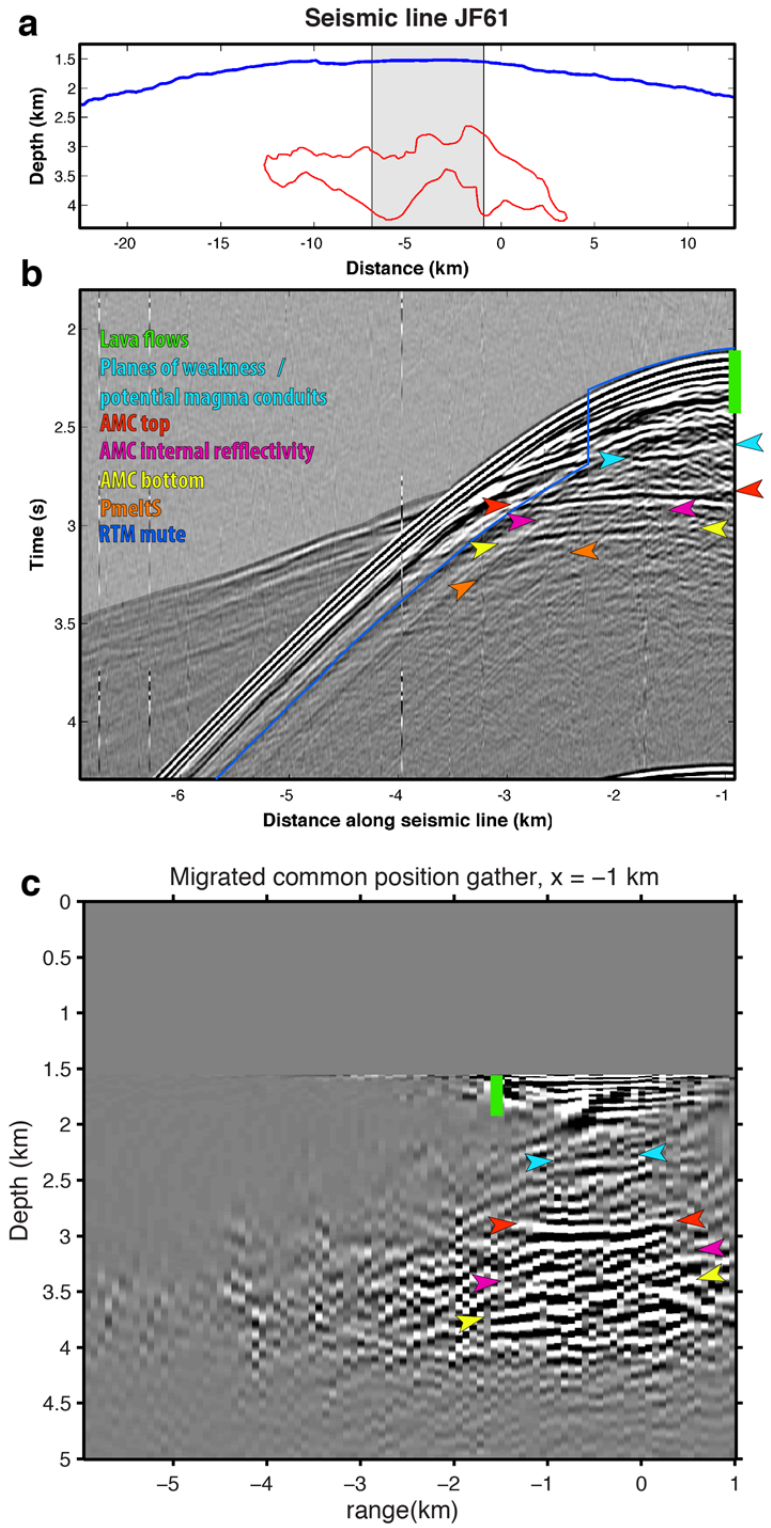

Figure DR2. Constructing the reverse time migrated image. a. Bathymetry (blue line) along seismic line 61 and location of shot gather #1867 from b. The red line outlines Axial volcano's magma reservoir b. Preprocessed surface shot gather band pass filtered using a seventh-order Butterworth band-pass filter with corner frequencies of 3 and 30 Hz to constrain the frequencies of the data to ones that satisfy the stability criterion of a 6.25 m finite-difference grid. The surface

data were convolved with $H(t)/\sqrt{t}$ (H being the Heaviside step function and t being the time) which boosted low frequencies with respect to high frequencies and with a predictive deconvolution filter to minimize the bubble pulse effect. The 6–km–long hydrophone streamer recorded significant amounts of near-vertical incidence energy from lava flows within the upper Layer 2A (green) as well as deeper crustal reflectors from the top and bottom of a large magma reservoir (red and yellow arrows), and from the magmatic plumbing system (cyan arrows). Some internal reflectivity (magenta arrows) within the magma reservoir suggests that the large magma reservoir is made of several imbricated melt sills. Converted S-wave (PmeltS) magma chamber reflections (orange arrows) suggest high-melt concentration within the southeastern part of the reservoir. We chose to mute the energy associated with Layer 2A/2B turning rays (blue line) prior to migration to improve the RTM imaging. The Layer 2A/2B caustics do not correspond to a true reflection event and thus cannot be focused correctly by the RTM algorithm (in a velocity gradient image). When reverse time migrated this energy produces a high-amplitude, low-frequency event that dominates the migrated image at the base of layer 2A. c. Migrated common position gather at -1 km along seismic line 61. The crustal events recognized on b. are presented using the same symbols. Flat events in a common position gather attest to the accuracy of the migration velocity model. Our FWI velocity model thus appears to be well constrained from seafloor depth down to the top of the magma chamber. The residual moveout of the magma reservoir bottom reflector suggests that velocities within the magma chamber are lower than those in the FWI model. While the reflection from the base of the magma chamber is unambiguously real, its corresponding energy is not completely focused in our final RTM images resulting in thickness estimates uncertainties.

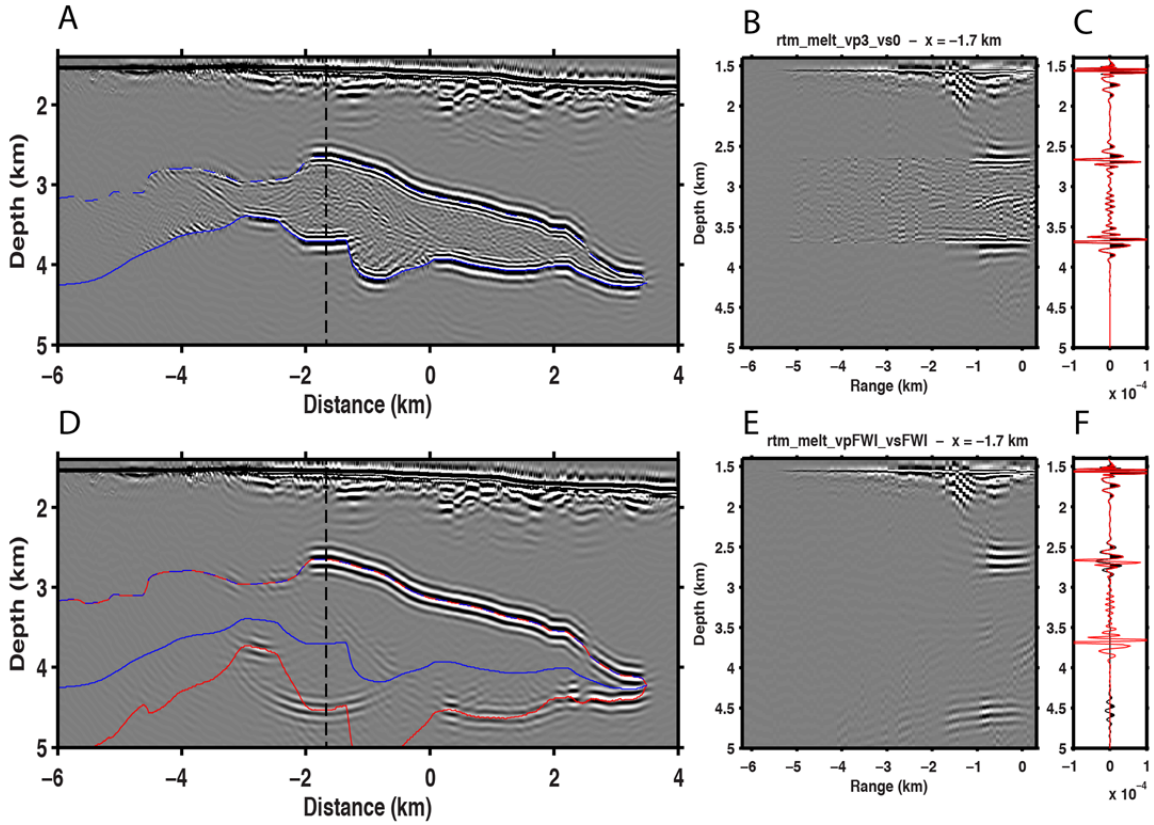

Figure DR3. Pitfalls of reverse time migration imaging using an incorrect velocity structure – results from a synthetic test. A total of 185 consecutives shots were modeled for a 2D synthetic

model created from the final FWI velocity structure along seismic line 61. A pure melt magma chamber (Vp = 3 km/s, Vs = 0 km/s) was incorporated in the model creating strong top and bottom reflection arrivals from the magma reservoir. A. RTM section created using correct ("known") background velocity structures. The blue line outlines the magma chamber. The dashed black vertical line shows the location of the common position gather shown in B. B. Migrated common position gather at -1.7 km along the seismic line. Most of the energy contributing to the magma chamber top and bottom reflectors is from near vertical incident angle (range between -1.5 km and 0 km). Both these reflectors are flat, because the migration velocity model is correct. C. The output created by summing data from the full offset range of the common position gather in B shown as a variable area plot and as a red line. D. RTM section created using the FWI model with incorrect velocities within the magma chamber. The top reflector is well imaged but the bottom reflector is not due to the higher velocities and the thickness of the magma reservoir. The red line is the predicted bottom reflector from traveltime delays of normal incident raypaths. E. Same as B. except for the FWI velocity model. While the upper magma chamber reflector is still well migrated, the residual moveout of the bottom reflection suggests incorrect magma chamber velocities. F. The variable area plot was created by summing the full offset range of the common position gather in E. while the red wiggle line is the response from B using the correct velocity structures.

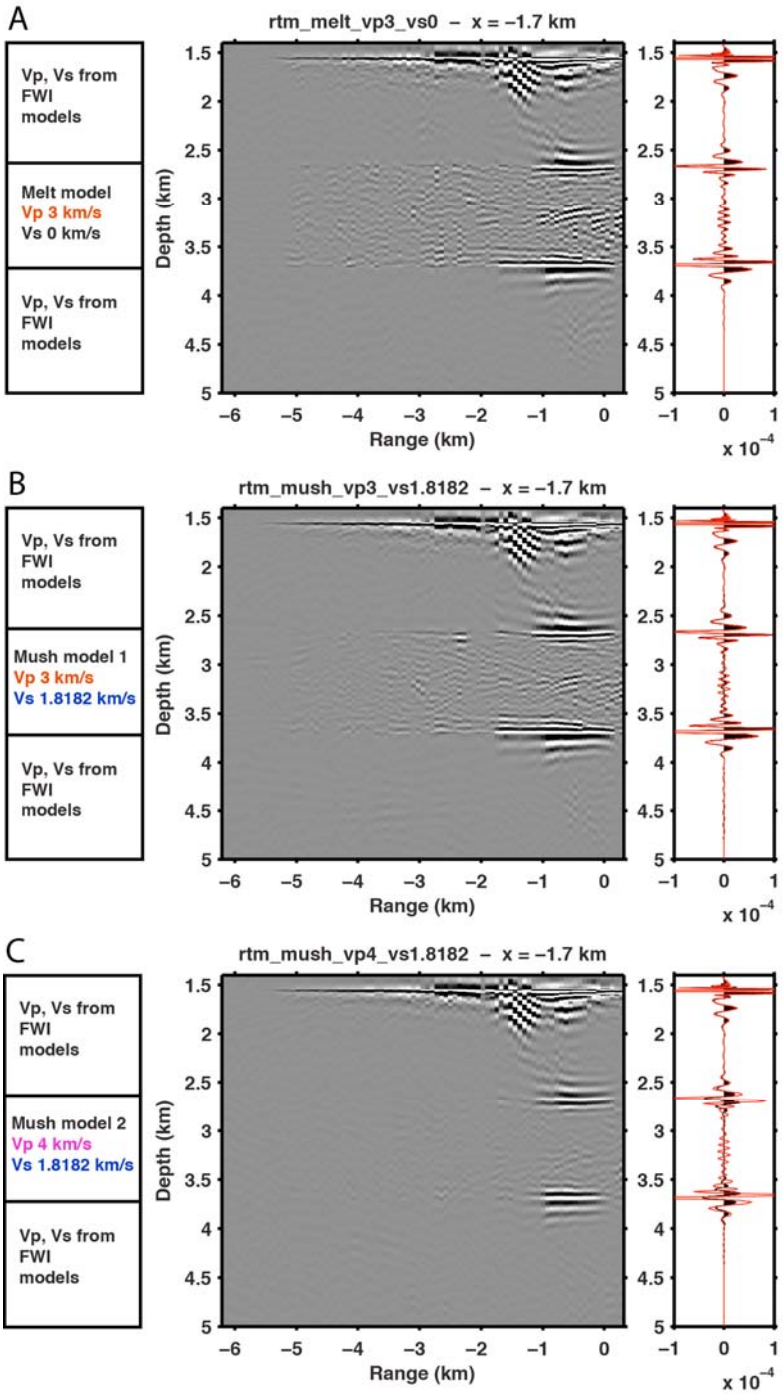

Figure DR4. Elastic P-wave reflectivity response from a melt or mush magma reservoir. The amplitude of the magma chamber in our RTM images, which correspond to the P-wave velocity gradient, are sensitive to changes in P-wave velocity but insensitive to the S-wave velocity structure. This behavior is illustrated here by test models that use the final FWI model along seismic line 61 except for introducing different magma chamber structures. RTM imaging used the correct model velocity in all cases A. "The pure melt case". A pure melt magma chamber (Vp = 3 km/s, Vs = 0 km/s; see *left panel*) was introduced within the model to create strong reflection

arrivals from the top and bottom limits of the magma reservoir. *Middle panel*: Migrated common position gather at -1.7 km. *Right panel*: The elastic P-wave reflectivity response of the "pure melt" created by summing the all offsets of the common position gather, black wiggle-variable area plot and red line. B. "Mush case #1". Similar to A except for a mush magma reservoir (Vp = 3 km/s, Vs = 1.8182 km/s; see *left panel*). *Right panel*: The black wiggle-variable area plot is the elastic P-wave reflectivity response of the "mush #1" magma reservoir, while red line is the response of the "melt" magma reservoir from A. C. "Mush case #2". Similar to A & B except for a mush magma reservoir (Vp = 4 km/s, Vs = 1.8182 km/s; see *left panel*). *Right panel*: The black wiggle-variable area plot is the elastic P-wave reflectivity response of the "mush #2" magma reservoir while the red line is again the "melt" magma reservoir from A for comparison.

The P-wave reflectivity response of the "pure melt case" and "mush case #1", which differ only in their S-wave velocity structures, are almost identical, but the response for "mush case #2" has lower amplitude than "mush case #2" because of the smaller P-wave velocity jump.